Investigation of the Li-Ion Insertion Mechanism for Amorphous and Anatase TiO_2 Thin-Films

S. Moitzheim,[1,2,*] S. De Gendt,[1,3,] and P. M. Vereecken[1,2,***,z]**

[1] *imec, B-3001, Belgium*
[2] *KU Leuven, Department of Microbial and Molecular Systems, B-3001 Heverlee, Belgium*
[3] *KU Leuven, Department of Chemistry, B-3001 Heverlee, Belgium*

Titania is considered an interesting anode candidate for Li^+-ion batteries, as it offers a high theoretical capacity (1280 mAh cm^{-3} or 336 mAh g^{-1}) and long term cycling stability. Unfortunately, the most commonly investigated anatase structure never reaches the theoretical capacity at practical charging rates (i.e. above 1 C). In this work, we compare amorphous (am-TiO_2) to anatase TiO_2 thin-films, and investigate the exceptional performance of am-TiO_2 as Li^+-ion insertion electrode. An in-depth electrochemical characterization using cyclic voltammetry (CV), constant current lithiation and delithiation, and potentiostatic intermittent titration technique (PITT) is performed. From CV, the insertion and extraction kinetics of am-TiO_2 is found to be unrestricted by diffusion, contrary to anatase. Based on our combined electrochemical results, two different mechanisms are formulated for anatase and am-TiO_2. Whereas anatase is filled from the "top-down", with a buildup of Li near the electrode/electrolyte interface, am-TiO_2 shows a "bottom-up" filling mechanism. This discrepancy is ascribed to the difference in diffusion coefficient measured for am-TiO_2 and anatase. This work highlights the differences of Li-ion insertion into amorphous TiO_2 compared to anatase, and gives guidance on material development for high capacity and fast charging electrodes.

 [DOI: 10.1149/2.1091816jes]

Manuscript submitted September 10, 2018; revised manuscript received November 30, 2018. Published January 2, 2019.

To meet the ever-growing demands for fast charging and high capacity energy storage, novel Li^+-ion battery materials are continuously being developed. Specifically for the negative electrode, high-rate performance materials are desired. As such, TiO_2 is an intriguing material, as it is abundant, environmentally benign, stable and has a high theoretical capacity of 336 mAh g^{-1} or 1280 mAh cm^{-3}. The most widely studied TiO_2 structure is the anatase polymorph. Li^+-ions can be inserted into TiO_2 with the consecutive reduction of Ti(IV) to Ti(III) redox centers, given as:

$$TiO_2 + xLi^+ + xe^- \leftrightarrow Li_xTiO_2 \quad [1]$$

with $0 \leq x \leq 1$. Unfortunately, bulk anatase exhibits a very poor rate-performance and in turn poor achievable capacity, with only about 770 mAh cm^{-3} (i.e. $x = 0.6$ or 200 mAh g^{-1}) that can be achieved at very low charging rates (<0.1 C). This poor performance is attributed to the combination of low electronic and ionic conductivity. There have been many strategies to achieve the full capacity ($x = 1$) and fast charging, such as nanosizing,[1,2] doping,[3,4] or carbon composites.[5,6] Nevertheless, even for the best performing anatase TiO_2 electrode, the capacity remains around 900 mAh cm^{-3} (235 mAh g^{-1} or $Li_{0.7}TiO_2$) at a charging rate of 1 C, and quickly fades to 380 mAh cm^{-3} (100 mAh g^{-1} or $Li_{0.3}TiO_2$) or below at rates of 10 C and higher.[1] To solve this, alternative TiO_2 structures or polymorphs have been investigated (e.g. TiO_2(B)).[7] Interestingly, amorphous TiO_2 (am-TiO_2) was also shown to achieve a higher capacity and rate-performance compared to anatase.[8–10]

In Table I, capacities for state-of-the-art TiO_2 electrodes are given (see Ref. 11 for a more complete overview of state-of-the art capacities). It shows that almost double the capacity can be reached with am-TiO_2 at a moderate charging rate of 3 C, while this becomes almost three-fold at a rate of 45 C (for the nanotubes). Am-TiO_2 was also combined with carbon nanosheets,[12,13] carbon nanotubes,[14] and carbon nanowires,[15] which resulted in high capacities and rate-performances. Interestingly, when using the amorphous structure, it seems that the rate-performance of TiO_2 is generally enhanced compared to the crystalline structures, with capacities around 500 mAh cm^{-3} (or 130 mAh g^{-1}) for C-rates in the range of 40 C.[8,9,13]

At present, although nanoscale am-TiO_2 shows promising results, detailed electrochemical characterization of the underlying kinetics of Li^+-ion insertion is lacking. Since it is often difficult to isolate the influence of electrode geometry (e.g. effective area, pore and particle size distribution, etc.) and electrode formulation (e.g. electronic additives and binder), the analysis of the underlying kinetics can be complex and ambiguous. To investigate the properties in a well-defined system, in this work, nanosized (≤35 nm) planar thin-films of am-TiO_2 and anatase were fabricated and characterized electrochemically. For the first time, nanosized am-TiO_2 thin-films have been characterized and directly compared to anatase TiO_2. Such am-TiO_2 thin-films could be applied as an electrode for three-dimensional thin-film batteries,[16] or as a surface protective coating for electrode particles (see e.g. Refs. 17 and 18).

As a deposition technique, atomic layer deposition (ALD) was used, which can deposit pin-hole free and uniform films over large surface areas with atom-level thickness control. By using different deposition precursors, amorphous and anatase films with controlled thickness were obtained. The structural and chemical composition was confirmed with grazing incidence X-ray diffraction (GI-XRD) and elastic recoil detection analysis (ERDA). The electrochemical properties of our nanoscaled amorphous and anatase TiO_2 films were characterized systematically by cyclic voltammetry, galvanostatic charge/discharge and the potentiostatic intermittent titration technique (PITT). The PITT results were analyzed using a method of numerical inversion of Laplace Transforms, which allowed the extraction of underlying transport properties such as (the potential dependent) diffusion and

Table I. Examples of the capacity of state-of-the-art anatase and amorphous TiO_2 structures.

Electrode	Gravimetric capacity (mAh g^{-1})	Volumetric Capacity* (mAh cm^{-3})	C-rate$^{\phi}$
3D ordered microporous anatase[1]	150	570	3
	116	440	6
Vertically aligned anatase nanotubes[9]	111	420	3
	50	190	45
Vertically aligned amorphous nanotubes[9]	229	870	3
	161	610	45

*Reports given in units of gravimetric capacity (mAh g^{-1}) were converted to volumetric capacities (mAh cm^{-3}) by assuming a density of 3.8 g cm^{-3}.
$^{\phi}$A rate of 1 C corresponds here to 336 mA g^{-1} or 1280 mA cm^{-3}.

*Electrochemical Society Student Member.
**Electrochemical Society Fellow.
***Electrochemical Society Member.
zE-mail: philippe.vereecken@imec.be

charge transfer coefficients. Together with the different electrochemical techniques, the enhanced capacity and rate-performance of am-TiO_2 is explained, and two distinct Li^+-ion insertion mechanisms for each structure are formulated.

Material and Methods

Substrate and TiO_2 deposition.—300 mm TiN-coated Si wafers were used as substrate for the TiO_2 films. Titanium nitride (TiN) was deposited on the Si substrate by ALD in a Pulsar 3000 reactor (ASM). Before deposition, the Si wafer was cleaned by an ozonated water rinse, followed by an HF/HCl based etch. TiN was chosen as it functions as current collector and diffusion barrier for lithium into the underlying Si.[19] Anatase was deposited directly on full 300 mm TiN-coated Si wafers in the clean room. For am-TiO_2, the TiN-coated Si wafers were manually cleaved in 2×2 cm^2 pieces. Amorphous and anatase TiO_2 films were deposited by ALD using two different processes. Am-TiO_2 films were deposited from a tetrakis dimethylamido titanium ($Ti(N(CH_3)_2)_4$ or TDMAT) and water precursor at 100°C in a custom built ALD reactor. TDMAT and H_2O were sequentially exposed to the TiN substrate for a total number of 700, 200 or 100 cycles, to deposit films with a nominal thickness of 35, 10 and 5 nm. The TDMAT process is chosen as it was known to form amorphous TiO_2 at a deposition temperature of 100°C.[20] Anatase films were deposited at 250°C using $Ti(OCH_3)_4$ and H_2O as precursors in a Pulsar 3000 reactor (ASM). A total number of 682 cycles (nominal thickness of 35 nm) were adopted, which leads to polycrystalline anatase films.[21] A short comparison between H_2O and O_3 as the oxygen source was made for anatase films in terms of electrochemical properties (see Figure S1). No significant difference was found between the two precursors, and H_2O was chosen for the remainder of the work. The film thicknesses of the 35 nm anatase and am-TiO_2 films were confirmed using scanning electron microscopy (SEM). From ERDA experiments on TiO_2/TiN samples, it was found that oxygen and carbon impurities were below 1 at.% in the TiN layer (see Figure S2 for ERDA depth profile), and the compositions of the TiO_2 films are given in the results section. The bulk resistivity of our ALD TiN was measured to be around 5×10^{-6} Ω m.

Structural and chemical characterization.—The amorphous nature of the am-TiO_2 films and crystallinity of the anatase films were determined by grazing incidence X-ray diffraction (GI-XRD) and visualized with transmission electron microscopy (TEM). The film composition was determined with elastic recoil detection analysis (ERDA). GI-XRD was performed with an X-Pert PRO MRD (Panalytical), equipped with a Cu Kα X-ray source. On the incident beam side, a graded parabolic mirror and a 1/32° divergence slit were inserted, and on the diffracted side, a 0.04 rad Soller slit together with a parallel plate collimator. GI-XRD measurements were done at an incidence angle of 1°, and the signal was continuously recorded by scanning in the 2θ direction at a rate of 0.025° s^{-1}. TEM was performed with a Titan G2 (FEI) at an operating voltage of 120 kV. For the TEM sample preparation, a spin-on-carbon and Pt capping layer was applied on top of the TiO_2 layer, and a slice of this stack was removed by a focused ion beam for further analysis. For ERDA, a Cl^{4+} ion beam is accelerated to an energy of 8.0 MeV, and impinged onto the sample, using a scatter angle of 40.5°.[22,23] Either incident ions elastically scattered from atoms in the sample, or host atoms elastically recoiled from the sample are detected by a time-of-flight energy telescope. The kinetic energy as well as the speed (time-of-flight) of each atom reaching the detector allows for the identification of the corresponding element in the film. For the analysis, the signal from recoiled atoms were used for all elements except titanium, which is determined from scattered Cl^{4+}. More information of our ERDA setup can be found in Ref. 14.

Electrochemical characterization.—A custom-made three-electrode polytetrafluoroethylene (PTFE) cell was used which is clamped onto the substrate using a Kalrez O-ring (exposed surface area of 1.1 cm^2) and filled with a liquid electrolyte (10–15 mL). The substrate is sandwiched between a copper foil and the electrochemical cell (see Figure S3). The cell contains two compartments, into which Li metal strips were placed, and which served as the counter and reference electrode. The compartment with the Li reference electrode was connected to the main compartment through a Luggin capillary close to the surface of the working electrode (at 4 mm). Electrical contact is made to the TiN current-collector by scratching the uncovered (Si) side of the sample and applying a Ga-In eutectic paste on the back and edges of the sample, which is then in contact with the copper foil. Note that an O-ring seal prevents the electrolyte solution from contacting the Si substrate and Cu/Ga-In/TiN current collectors (see Figure S3), thus preventing any insertion or alloying reactions to occur with these components. All experiments were performed at room temperature (21°C) using a $LiClO_4$ in propylene carbonate (PC) electrolyte solution. For ease of preparation, an ampoule containing $LiClO_4$ (100 g, battery grade, dry, 99.99%, Sigma Aldrich) was dissolved in propylene carbonate (100 mL, 99.7%, Sigma Aldrich), which results in a 0.94 M solution. The substrate edges were softly scratched and covered with a silver paste to contact the TiN current collector. Measurements were done in an Ar filled glove box with O_2 and H_2O levels below 1 ppm. The electrochemical cell was controlled through a PGSTAT101 Autolab (Metrohm) potentiostat/galvanostat, using the Nova 1.10 software. Cyclic voltammetry was performed between 1.0 V and 3.2 V or 0.1 and 3.2 V, with scan rates ranging from 1 mV s^{-1} to 100 mV s^{-1}. Constant current lithiation and delithiation experiments were done with charging rates (C-rate) between 1 C and 500 C. A rate of 1 C is based on the theoretical capacity of anatase as determined from the Ti content from ERDA and by assuming the reduction of Ti(IV) to Ti(III). PITT was performed in the voltage range of 3.0–1.0 V, with potential step increments of ±10 mV. Each consecutive step was applied after a cutoff current of ±0.44 μA cm^{-2} (~0.1 C) was reached. All potentials are given vs Li^+/Li.

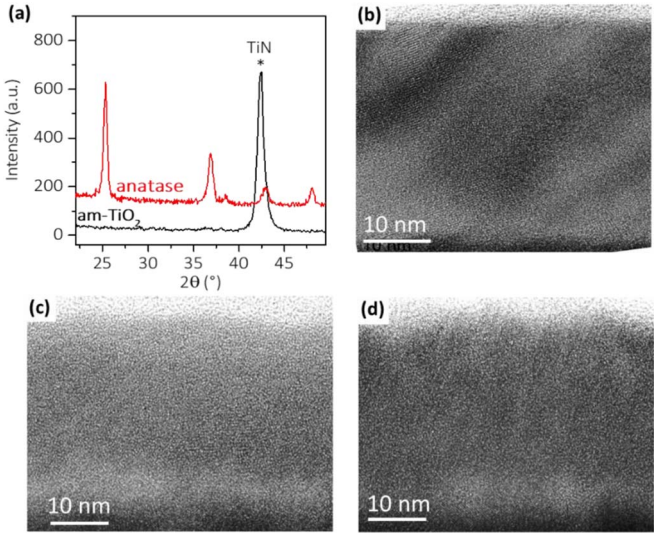

Figure 1. (a) Grazing incidence XRD of 35 nm am-TiO_2 and anatase films. Star denotes the signal from the TiN current collector. TEM image of an anatase TiO_2 film as deposited (b), an am-TiO_2 film as deposited (c), and an am-TiO_2 film after electrochemical testing (d).

Results

Structure and composition.—The crystallinity of the TiO_2 films was examined by GI-XRD (Figure 1a). The 35 nm anatase film show the characteristic diffraction peaks for the (101), (103) and (200) crystal planes, at 2ϑ angles of 25.3°, 36.8° and 48.1°, respectively. On the other hand, the 35 nm am-TiO_2 film is devoid of clear features, besides a peak related to the TiN current collector at 42.5°, which

Table II. Composition of the 35 nm anatase and am-TiO_2 films as determined by ERDA. The maximum capacity is calculated from the Ti content by assuming a complete reduction of Ti(IV) to Ti(III).

	Anatase	am-TiO_2
H (at.%)	0.4	6.9
C (at.%)	0.3	2.0
N (at.%)	0.1	2.2
O (at.%)	61.9	55.6
Ti (at.%)	37.3	33.3
Ti content (10^{15} at. cm^{-2})	97	61
Max. capacity (mAh cm^{-3})	1230	770

confirms the amorphous nature of the TiO_2 film. TEM analysis of anatase and am-TiO_2 films was also performed. Figure 1b shows the as-deposited anatase thin-film. The polycrystalline anatase structure is clearly revealed. Crystalline grains are detected that span the full thickness of the TiO_2 layer and are 50 to 100 nm in length. Lattice distances obtained after Fast Fourier transform of crystalline regions were matched to the anatase structure. Cross-sectional TEM images of am-TiO_2 were made for as-deposited films (Figure 1c) and for samples after electrochemical testing (Figure 1d). Both for as-deposited and electrochemically cycled am-TiO_2, the structure is seen to be mainly amorphous. Only for a few images, some small crystalline regions were detected (<5 nm), and were indexed to a rutile TiO_2 structure. Overall the am-TiO_2 samples are amorphous and remained so even after electrochemical cycling.

The compositions determined by ERDA of the 35 nm films are given in Table II. For the anatase film, the O:Ti ratio is 1.7, which shows that the films are oxygen deficient. Also, hydrogen, carbon and nitrogen contamination are below 0.4 at.%. For the am-TiO_2 film, an O:Ti atomic ratio of 1.7 is also measured. In this case, several at.% of hydrogen, carbon and nitrogen impurities are detected, which likely originate from incomplete removal or partial decomposition of the $-N(CH_3)_2$ ligand during the deposition.

The total Ti content for am-TiO_2 is considerably lower than that of the anatase film even though they have the same thickness, indicating a lower density of the amorphous film. Based on the Ti content, the density for the anatase film was calculated at 3.7 g cm^{-3}, which is close to the theoretical density of 3.8 g cm^{-3},[24] and 2.3 g cm^{-3} for am-TiO_2. Assuming that 1 Li per Ti can be inserted (i.e. reduction from Ti(IV) to Ti(III)), this corresponds to a maximum capacity of 1230 and 770 mAh cm^{-3} (i.e. 336 mAh g^{-1}) for these anatase and am-TiO_2 films, respectively.

Cyclic voltammetry study of Li^+-ion insertion and extraction.— For the first electrochemical tests, cyclic voltammetry (CV) measurements were done in two different potential ranges: 3.2–1.0 V, and 3.2–0.1 V. Fresh anatase and am-TiO_2 films (35 nm thickness) were cycled three times in these potential ranges (Figure 2). During the first three cycles in Figure 2a, anatase films shows a typical reduction peak around 1.6 V, which corresponds to Li^+-ion insertion (Eq. 1). A small shoulder is apparent after the peak at 1.6 V, which is also typically seen for anatase TiO_2.[25] For subsequent cycles in the same potential range, the current in the cathodic region slightly diminishes, which can be attributed to the reduction of surface bound water or decomposition of the electrolyte solution. On the anodic side, a peak around 2.2 and 2.4 V is measured, for the anatase samples scanned to 1.0 and 0.1 V, respectively, which is attributed to Li^+-extraction. Scanning to 0.1 V results in lower peak current densities for lithiation and delithiation, and shifts the delithiation peaks to a higher potential. On the other hand, from the charge measured during the cathodic and anodic scans, it is found that approximately 30% more lithium can be inserted and extracted into anatase when scanning to 0.1 V. Interestingly, when more lithium is inserted, the delithiation potential is shifted to higher values with broadening of the anodic peak, which suggests a more sluggish delithiation kinetics.

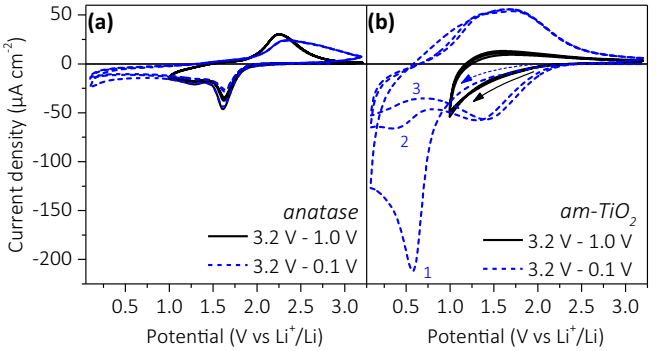

Figure 2. Cyclic voltammograms of 35 nm anatase (a) and am-TiO_2 (b) films cycled 3 times in the range of 3.2–1.0 V, and 3.2–0.1 V at 10 mV s^{-1}. Measurements were done in a three-electrode setup using a Li metal counter and reference electrode, and a 1 M $LiClO_4$ in PC electrolyte solution.

The CV scans for am-TiO_2 show a quite different behavior compared to anatase (Figure 2b) and the selected potential range now affected the shape of the voltammogram. Am-TiO_2 cycled down to 1.0 V showed no clear peak features in both the cathodic and anodic regions. Subequent scans did not alter the current response. However, when scanned down to 0.1 V the am-TiO_2 was activated with a large cathodic peak at 0.57 V in the first scan. In the reverse scan, a broad anodic peak at 1.6 V for delithiation of am-TiO_2 film is observed, which returns reproducibly in the following scans. Interestingly, from the second cycle on, a reproducible cathodic peak also appears at 1.5 V and is attributed to Li^+-ion insertion upon reduction of Ti(IV) to Ti(III). The peak around 0.57 V is still present, albeit 200 mV shifted more negative and quickly reduces in intensity upon cycling. A much larger capacity of −1170 mAh cm^{-3} under the cathodic peak at 0.5 V in the first scan versus the +600 mAh cm^{-3} in the anodic scan, points to an irreversible component in the first activation scan. At this point, the exact reaction is unclear, however it must involve some transformation of the amorphous material as merely the formation of an SEI layer cannot explain the activation behavior. Activation of amorphous ALD deposited thin films has been observed also for other material systems.[26,27] For the remainder of the CV analysis, a voltage range of 3.2–0.1 V was adopted.

To further investigate the lithium insertion and extraction kinetics, additional CV experiments of 35 nm am-TiO_2 and anatase films were performed in the 3.0–0.1 V range at varying scan rates between 1 and 100 mV s^{-1} (Figure 3). The 10, 20, 50 and 100 mV s^{-1} scans are shown for am-TiO_2 (Figure 3a) and anatase (Figure 3b) films. Note that since am-TiO_2 resulted in higher current densities, the scale of the "current density" axis for am-TiO_2 (Figure 3a) is four times larger than for anatase (Figure 3b). First, the peak potential as a function of scan rate is examined for am-TiO_2 (Figure 3c), and anatase (Figure 3d). For am-TiO_2, at low scan rate, the lithiation and delithiation peak potentials are very close, (1.75 V for lithiation and 1.81 V for delithiation at 1 mV s^{-1}), with an average peak potential, $U_{av} = (U_{lith} + U_{delith})/2$, of 1.78 V. The average potential of am-TiO_2 is very near the average potential measured with PITT (see next section), which is about 1.77 V. The average peak potential at low scan rates corresponds to the standard redox potential of the insertion/extraction reactions. Upon increasing the scan rate, mostly the lithiation peak potential shifts to more negative values, which also shifts the average potential. Shifting peak potentials are related to overpotentials induced by charge-transfer resistance and other ohmic resistances such as the ionic and electronic resistance of the electrode. A shift in the average peak potential indicates that the lithiation and delithiation reactions no longer follow Nernstian equilibrium conditions. For am-TiO_2, the cathodic peak potentials shift significantly more than the anodic peak potentials, which shows that lithiation is more kinetically hindered than delithiation. The peak potentials of anatase (Figure 3d) are shifted compared to am-TiO_2, with peak potential values at 1.69 V and 2.26 V (1 mV s^{-1}),

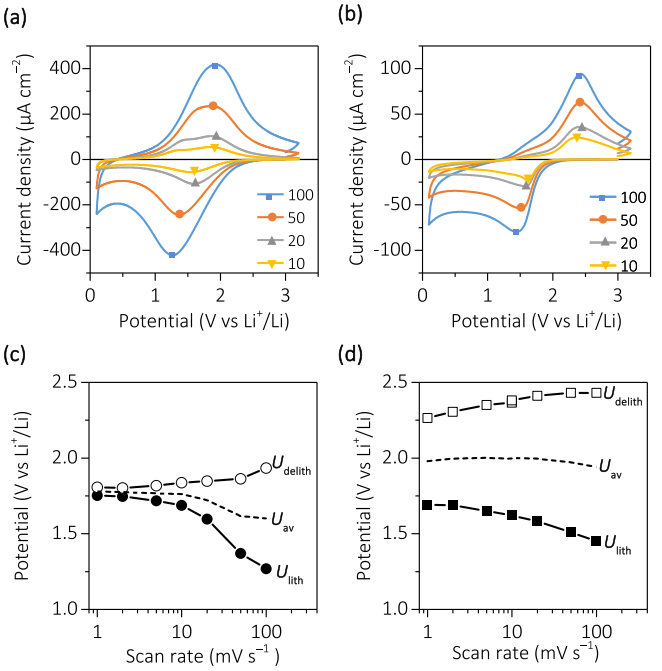

Figure 3. Cyclic voltammetry experiments of 35 nm am-TiO_2 and anatase films. Scans recorded at 10, 20, 50 and 100 mV s^{-1} are shown for am-TiO_2 (a) and anatase (b). The peak potential as a function of scan rate for am-TiO_2 (c) and anatase (d). The films were cycled between 3.2 and 0.1 V.

for lithiation and delithiation, respectively. The crystalline anatase has potentials determined by a two-phase transformation equilibrium[28] whereas amorphous titania follows Nernstian behavior as for solid solutions. Indeed, there is a significant separation in the cathodic and anodic peak potential of about 0.57 V (at 1 mV s^{-1}) for anatase, whereas this is only few tens of millivolts (~50 mV) for am-TiO_2. The average peak potential (standard redox potential) of anatase at this low scan rate (1.98 V) is about 0.2 V more positive than for am-TiO_2 (1.8 V) showing that they have different thermodynamic properties as well.

The scan rate dependence of the lithiation peak currents ($i_{p,lith}$) for amorphous and anatase films are investigated in Figure 4a. In general, the peak current density for am-TiO_2 is higher than anatase. Importantly, the peak currents for am-TiO_2 are linearly dependent with scan rate (i.e. a slope of 1.0 in the log-log plot), while anatase shows a near-square root dependency (i.e. a slope of 0.58). Hence, insertion is not limited by solid-state diffusion for am-TiO_2, ($i_{p,lith} \propto \nu$), while it

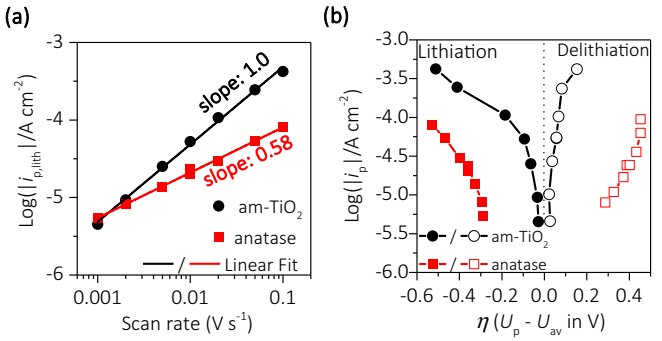

Figure 4. The logarithm of (lithiation) peak currents vs scan rate (a), and (lithiation and delithiation) peak currents vs overpotential (b) for 35 nm am-TiO_2 and anatase films. The overpotential was calculated by subtracting the lithiation and delithiation peak potentials with the average potential. The electrodes were cycled between 3.2 and 0.1 V.

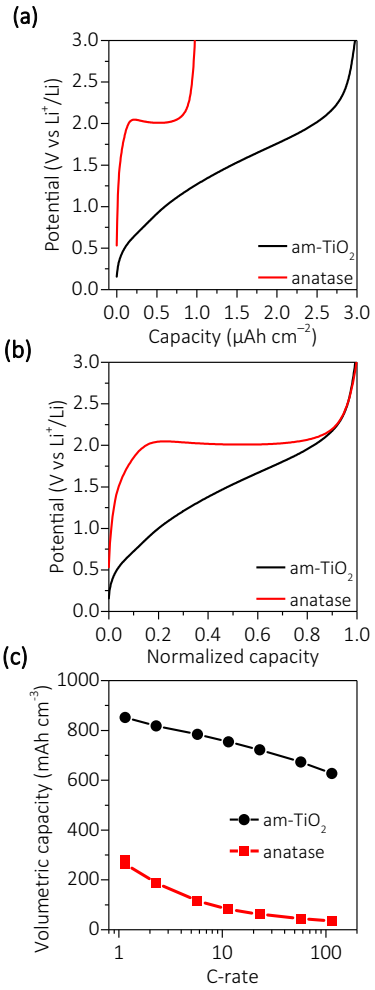

Figure 5. Charge/discharge experiments for 35 nm anatase and am-TiO_2 films. (a) The potential vs capacity during delithiation for anatase and am-TiO_2. (b) The potential vs normalized capacity (i.e. the capacity divided by the total capacity reached at 3.0 V). (c) The volumetric capacity of anatase and am-TiO_2 as a function of C-rate. A rate of $n \cdot$ C corresponds to $n \cdot$ 4.3 μA cm^{-2}. The cutoff voltages were 0.1 and 3.0 V, for lithiation and delithiation, respectively.

is for anatase ($i_{p,lith} \propto \sqrt{\nu}$).[29,30] This suggests that the average Li^+-ion diffusion coefficient is higher for am-TiO_2 than for anatase, since the maximum diffusion distance for Li^+-ions is the same in both films. The behavior of the diffusion coefficient as a function of electrode potential will be analyzed in more detail by PITT in the next section. The peak currents were also plotted as a function of overpotential (η) in Figure 4b. The lithiation and delithiation overpotentials were determined by subtracting the average or formal potential determined at the lowest scan rate from the measured peak potentials. The plot reveals that for both the lithiation and the delithiation reactions, am-TiO_2 requires a smaller overpotential to achieve a certain peak current, suggesting overall more facile kinetics compared to anatase.

Rate-performance probed by constant current charge/discharge.—The rate-performance of the 35 nm anatase and am-TiO_2 films were probed by constant current lithiation and delithiation experiments (Figure 5). Typical potential-capacity profiles for delithiation at 1 C rate are shown in Figure 5a. The lithiation and delithiation steps were performed at the same current density or C-rate. The cutoff potential was 0.1 V and 3.0 V for lithiation and delithiation, respectively. For the analysis, only the delithiation curves were considered to assess the reversible charge stored. The potential-capacity profiles

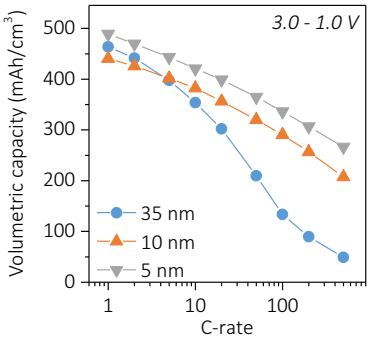

Figure 6. Volumetric (delithiation) capacity of 35, 10 and 5 nm am-TiO_2 films as a function of C-rate. A rate of n·C corresponds to $n \cdot 4.3$, $n \cdot 1.2$ and $n \cdot 0.61$ μA cm^{-2} for the 35, 10 and 5 nm films, respectively. The rate-performance was measured in a custom built three-electrode cell.

of Figure 5a show quite some differences, and a significantly higher capacity for am-TiO_2 compared to anatase.

For easier comparison of the potential profile shapes, we normalized the capacities to their maximum value upon reaching the cutoff potential (Figure 5b). The potential profile of anatase shows a clear plateau at 2.0 V typical for a two-phase transformation reaction, whereas am-TiO_2 shows a sloped profile across the full potential range, resembling a a solid solution type insertion. Also, about 20% of the total Li^+ is inserted/extracted below 1.0 V for am-TiO_2, while only a small fraction is inserted below 1.0 V for anatase TiO_2. The C-rate performance of 35 nm thick anatase and am-TiO_2 films is shown in Figure 5c. At 1 C, anatase reaches 285 mAh cm^{-3} (i.e. 77 mAh g^{-1} or $Li_{0.24}TiO_2$), while am-TiO_2 achieves 851 mAh cm^{-3} (370 mAh g^{-1} or $Li_{1.1}TiO_2$). The stoichiometry of $Li_{1.1}TiO_2$ for am-TiO_2 could mean that more than 1 Li/Ti is inserted, or that ERDA slightly underestimated the Ti content (by 10%). It is likely that the latter is the case, as it is known that the ERDA signal for Ti is less accurate than for the heavier elements (at least 4% error is expected). At a rate of 115 C, the accessible capacity for anatase decreases to 11% of the maximum capacity, whereas this is still 67% for am-TiO_2; i.e. about 18 times higher. The enhanced rate performance of am-TiO_2 corroborates well the CV results.

The dependence of film thickness on the rate-performance was investigated for am-TiO_2 films only. Charge/discharge experiments were performed with 35, 10, and 5 nm thin am-TiO_2 films for C-rates between 1−500 C in the voltage range of 3.0–1.0 V to limit the background current which was most prominent for the thinnest film (Figure 6). For comparison, the 35 nm am-TiO_2 films show a volumetric capacity of about 450 mAh cm^{-3} (196 mAh g^{-1} or $Li_{0.58}TiO_2$) at 1 C in this voltage range. Interestingly, the 35 nm films show a rapid drop in capacity for C-rates larger than 10 C with only 10% of the maximum capacity remaining at 500 C. The thinnest films of 10 and 5 nm am-TiO_2, on the other hand, show a smooth and gradual decrease in capacity with C-rate with 50% of the capacity remaining at 500 C. Hence, at these high C-rates, the 5 and 10 nm have about 5 times the volumetric capacity of a 35 nm film.

The C-rate performance improves as the thickness of the films decreases. This follows from the shorter Li diffusion path for the thinner films. Whereas the CV results showed that the 35 nm films were not limited by bulk diffusion (determined by the peak current), the charge/discharge results show that the delithiation rate is still limited for currents >40 μA cm^{-2}. This indicates that diffusion may be still limiting at higher charges (Li loadings) than those at the peak current in the cyclic voltammograms. This can be illustrated when plotting the current against lithium loading obtained with the CV experiments (see Figure S4). Since the Li-ion transport properties depend on the Li content (see next section), it is possible that a CV can show no indication of diffusion limitation (i.e. at the peak current), whereas this is still observed in a charge/discharge experiment which probes a much wider capacity range.

The rate-performance of the 10 and 5 nm films is similar and the continuous change in Figure 6 indicates that the kinetics remains fast for all Li loadings. The mechanism for Li insertion and extraction will be discussed further on.

Determination of kinetic parameters by PITT.—The kinetics of the 35 nm am-TiO_2 and anatase films was studied in more detail using potentiostatic intermittent titration technique (PITT). The electrode potential is stepped in small potential increments of 0.01 V, and subsequent current transients are recorded until the new equilibrium Li-content at the new potential is reached. Since only a small perturbation is applied, the system can be considered in near-equilibrium state. PITT measurements were performed in the voltage range of 3.0–0.1 V for am-TiO_2 and 3.0–1.0 V for anatase as insertion/extraction is negligible for the latter below 1 V (see Figure 5a).

A series of current transients is shown for a selected potential range for am-TiO_2 (Figure 7a) and anatase (Figure 7b). Overall, the current transients for am-TiO_2 and anatase show a quite different response. For am-TiO_2 an exponential-like current decay is measured for each consecutive step over the whole potential range. For anatase, most of the current flows during a certain series of potential steps in a specific potential region. Furthermore, the current spikes are lower, and the time of subsequent steps varies considerably; i.e. from a few seconds to a few thousands seconds. During these long current transients, the current shows a phase nucleation-like behavior, which is marked by first a quick fall, then rise, and finally it falls again as it evolves over time. The incremental charge passed after each potential step is plotted against the electrode potential (Figures 7c–7d). For am-TiO_2 (Figure 7c), lithium ions are inserted and extracted broadly across the whole potential range, with broad peaks centered at 1.77 V for both the incremental insertion and extraction capacity. The peak positions and shapes are very similar to those seen in the cyclic voltammograms and confirms a solid-solution type insertion-extraction. Below 0.5 V an irreversible charge is seen, which points to the contribution of electrolyte solution decomposition at these low potentials. For anatase (Figure 7d), most of the lithium ions are inserted at 1.78 V and extracted at 1.90 V. This is a result of the sudden onset of phase transition between the lithium rich and lithium poor phase.

The potential-capacity profile is obtained from the integrated charge (vs applied potential) during the PITT experiment. The lithium-ion content (x in Li_xTiO_2) is shown as a function of potential for am-TiO_2 in Figure 7e. The profile is similar to the one obtained during the charge/discharge experiment (see Figure 5a). A stoichiometry up to $Li_{0.98}TiO_2$ is obtained during lithiation. A discrepancy between the lithiation and delithiation charge is observed: only 0.87 Li/Ti is extracted during the delithiation step. This is likely attributed to the irreversible component introduced by the electrolyte decomposition at low potentials. There is also slightly less lithium inserted/extracted during PITT compared to the charge/discharge experiment. This could be attributed to some experimental error introduced by the low current (nA) measurements, or an internal self-discharge phenomenon related to the solvent/electrolyte decomposition at low voltage. Alternative, it is possible that lithiation/delithiation of am-TiO_2 at such a slow rate leads to some degradation of the material. The potential-capacity profile reproduced from the cumulated charge of the PITT experiment for anatase (Figure 7f) also matches our previous charge/discharge results (see Figure 5a). Lithium-ions are reversibly inserted/extracted up to $Li_{0.44}TiO_2$ (1.89 μAh cm^{-2}). In this case, a higher capacity was obtained for the PITT experiment. Since the charge/discharge experiments for anatase were likely diffusion limited at 1 C, it follows that the slower PITT enabled more Li^+-ions to be inserted/extracted. It is known that the amount of solid-solution insertion into anatase (before phase transition occurs) depends on its particle size.[31] In our case, the Li-insertion proceeds up to a stoichiometry of $Li_{0.034}TiO_2$ before phase transition occurs at 1.78 V. This is similar to what Wagemaker et al. have shown for bulk anatase particles (i.e. 120 nm in size).[31] From previous reports, the phase transition results in an orthorhombic $Li_{0.5}TiO_2$ phase. In our case, after the nucleation-like current transient (i.e. below 1.78 V), an average stoichiometry of $Li_{0.12}TiO_2$ is

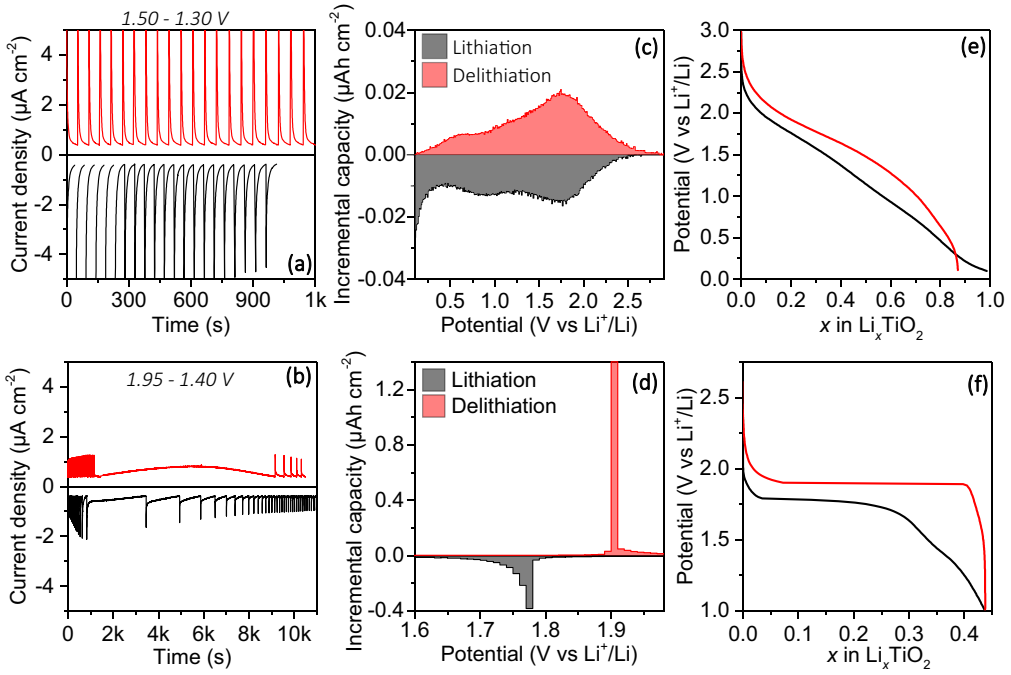

Figure 7. PITT experiments of lithiation (black) and delithiation (red) of 35 nm am-TiO_2 (a,c,e) and anatase (b,d,f) films. A selection of current transients in the potential range of 1.30 to 1.50 V for am-TiO_2 (a), and 1.40 to 1.95 for anatase (b) are shown. The time was shifted so that $t = 0$ equals the first point in the potential range of interest. The incremental capacity measured after each potential step is plotted vs the potential (c,d). The capacity (given as x in Li_xTiO_2) is plotted vs. the potential (e,f). For the PITT experiments, a potential step of ±0.01 V was applied until a cutoff current of ±0.44 μA cm^{-2} was reached.

obtained for anatase, suggesting that not all crystallites transformed to the $Li_{0.5}TiO_2$ phase. At the end of lithiation (at 1 V), the stoichiometry reaches $Li_{0.44}TiO_2$.

By analyzing the current transients, information on the near-equilibrium transport properties can be obtained.[32] Analytical solutions to the current transient are available for simple cases, for example based on assumptions of only semi-infinite diffusion (i.e. Cottrell equation),[33,34] or finite-length diffusion with or without inclusion finite reaction kinetics.[35,36] Often, graphical methods are used to determine diffusion time constants by finding maxima in $It^{1/2}$ vs t plots (the "Cottrellian region").[32] The graphical method can be expanded to include effects of slow reaction kinetics by plotting $(It^{1/2})^{-1}$ vs $t^{-1/2}$ for example, and fitting a linear function to the short time domain.[37] A problem that arises with such graphical methods, is the often arbitrary selection of the timespan used for fitting and oversimplification of underlying transport phenomena. A slightly more complicated, but vastly more powerful method, is the use of numerical inversion of Laplace transforms (NILT), as shown for example by Montella et al.[38–40] With this method, equivalent circuit models typically used for electrochemical impedance fitting can be transformed from the frequency domain to the time domain, and subsequently fitted by standard non-linear regression of I vs t data (see Figure 8). For example, NILT of the Warburg diffusion impedance is equivalent to the Cottrell equation. The advantage is that any arbitrary model expressed in terms of Laplace functionals can be used, and that the complete time domain can be represented (as opposed to the graphical methods). As the algorithm for NILT, the Gaver-Stehfest method[38] is used and implemented in the Mathematica software package,[41] together with a non-linear regression procedure.

All models suggested in Ref. 42 were tested with our data, such as the model representing finite reaction kinetics together with finite-length Warburg diffusion (FLW) or anomalous diffusion (trapping and release of ions). The model that best fitted our current transients ($0.005 < \chi 2 < 0.1$ for I vs t in μA), is shown in the inset in Figure 8. This relatively simple model consists of a "internal" resistor (R_Ω), Warburg diffusion element (W) and intercalation capacitance (C_{int}) in series. R_Ω is the sum of charge-transfer resistance (R_{ct}), series resistance (R_s) and electronic resistance of TiO_2 itself (R_e). From separate experiments, the series resistance is found to be below 100 Ω cm^2. The Warburg diffusion element has the Warburg coefficient, σ_W, which, together with the intercalation capacitance (C_{int}) is used to determine the diffusion coefficient. The intercalation capacitance is defined as:[32]

$$C_{int} = \Delta q / \Delta U \qquad [2]$$

where Δq is the incremental charge density integrated under the current transient and ΔU the applied potential step. C_{int} can either be determined as a fitting parameter, or directly by measuring the charge from the I vs t plot and dividing by the potential step. As a self-consistency check, the fitted value of C_{int} should be about the same as the measured one. In our case, the fitted C_{int} was about 1 to 4 times higher than the experimental one (see Figure S5), which is a relatively good match. The diffusion coefficient is given by:[35]

$$D = \frac{l^2}{(\sigma_W C_{int})^2} \qquad [3]$$

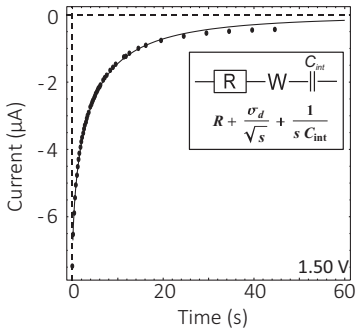

Figure 8. Example of a current transient of 35 nm am-TiO_2 film stepped from 1.51 V to 1.50 V. The solid line shows the fitted model based on the equivalent circuit (inset) transformed from the s-domain to the time domain using NILT. For this fit, a χ^2 value of 0.090 (for I vs t in μA) was obtained.

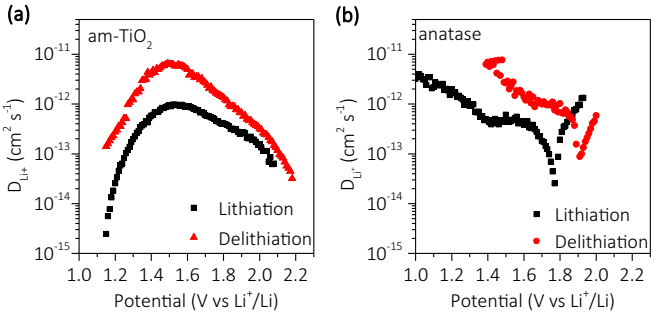

Figure 9. Diffusion coefficients obtained after fitting current transients using models obtained from NILT. The diffusion coefficients are based on the Warburg coefficient and intercalation capacitance, and given as a function of electrode potential for 35 nm thick am-TiO_2 (a) and anatase (b) films.

with l the thickness of the electrode film. This model was successfully applied to the current transients of lithium insertion and extraction in our am-TiO_2 films in the voltage range of 3.0–1.0 V. For anatase TiO_2, the same model was used, but with omission of C_{int}, as reliable values could not be obtained. In this case, the following analytical solution is available:[43]

$$I\ (t) = \frac{\Delta U}{R_\Omega}\ \exp\left(\frac{\sigma_W^2}{R_\Omega^2}t\right)\ \mathrm{erfc}\left(\frac{\sigma_W}{R_\Omega}\sqrt{t}\right) \qquad [4]$$

with fitting parameters R_Ω and σ_W as given above. Using the fitting procedures introduced above, R_Ω, σ_W and C_{int} were determined (see Figure S5—6) and the chemical diffusion coefficient as a function of electrode potential was determined using Eq. 3 for am-TiO_2 (Figure 9a) and anatase (Figure 9b). Note that for anatase, the previously discussed phase nucleation-like transients are not described by the models introduced above, and are therefore omitted from the analysis (i.e. at 1.78 for lithiation and 1.90 for delithiation).

From Figure 9a, the diffusion coefficient of am-TiO_2 is shown to vary between 10^{-11} and 10^{-15} $cm^2\ s^{-1}$ depending on the electrode potential. Specifically, maxima in diffusion coefficient near 1.5 V of 1×10^{-12} $cm^2\ s^{-1}$ and 6×10^{-12} $cm^2\ s^{-1}$ are found for lithiation and delithiation, respectively, for which the electrode has the composition of $Li_{0.34}TiO_2$ (lithiation) and $Li_{0.49}TiO_2$ (delithiation) The potential where the maxima occur are close to the peak potentials from CV and the maxima in incremental charge from PITT (Figure 7c). For anatase (Figure 9b) the diffusion coefficient varies between 10^{-11} and 10^{-15} $cm^2\ s^{-1}$ depending on the electrode potential, with sharp minima near the insertion (i.e. 2.6×10^{-14} $cm^2\ s^{-1}$) and extraction (8.8×10^{-14} $cm^2\ s^{-1}$) peaks. Although values for the diffusion coefficients of am-TiO_2 and anatase span the same order of magnitude, near the peaks of insertion and extraction, the diffusion coefficient of am-TiO_2 is several orders of magnitude higher. Besides a higher diffusion coefficient, am-TiO_2 also shows an internal resistance that is about ten times lower compared to anatase (see Figure S5—6). As can be seen, the PITT analysis allowed the determination of both the diffusion coefficient as well as the internal resistance, while the CV analysis gave only an indication of the limiting process (diffusion or charge-transfer). Note that although the same PITT model was used to fit the current transients for both films, a striking difference in the D versus U relationship is revealed (i.e. a maximum for am-TiO_2 and minimum for anatase in D vs U). The higher diffusion coefficient for am-TiO_2 at the peak of Li^+-ion insertion/extraction, together with the low charge-transfer resistance, explains the superior performance as seen from CV and rate-performance experiments.

Lithium insertion/extraction mechanisms.—Based on the previous results, we expect that Li^+-ion insertion and extraction mechanism is different for am-TiO_2 than for anatase. First anatase is considered, as it follows a behavior more typical for Li^+-ion insertion materials. From the CV results, Li^+-ion insertion kinetics of anatase was found to be dominated by diffusion. A schematic of this process is given in Figure 10a, which shows the Li concentration profile in the electrode during lithiation. Note that the concentration drawn in the schematic considers the insertion of both Li^+ and the accompanying electron, i.e. the reduced Ti(III) indicated by $Li_xTi^{4-x}O_2$, and we will refer this combined state as the Li concentration.

In the case of anatase, three different stages can be identified as x (in Li_xTiO_2) increases:

Solid-solution insertion (i.e. x << 0.034).—When TiO_2 is (nearly) empty (t_0), Li^+-ions are inserted via relatively fast solid-solution, leading to a nearly homogenous Li concentration profile throughout the film. As measured with PITT, the diffusion coefficient is near its maximum for low values of x ($>10^{-12}$ $cm^2\ s^{-1}$). In this case, the characteristic diffusion time ($\tau_D = l^2/D$) is in the order of tens of seconds.

Phase transition (x ≤ 0.034).—As $x \rightarrow 0.034$, the diffusion coefficient drops dramatically ($< 10^{-14}$ $cm^2\ s^{-1}$) and Li builds up within TiO_2 near the electrode/electrolyte interface. A characteristic diffusion time in the order of 1000's of seconds is obtained. As x = 0.034 (t_2), phase-transition initiates segregation of Li-ions at the top of the electrodes to form a Li-rich orthorhombic $Li_{0.5}TiO_2$ domain. Any additional Li moves the Li-rich phase further into the empty TiO_2 phase (t_3).

Lithium accumulation at the top of the electrode (x > 0.034).—If the Li flux into TiO_2 is higher than the moving $Li_{0.5}TiO_2$ phase can

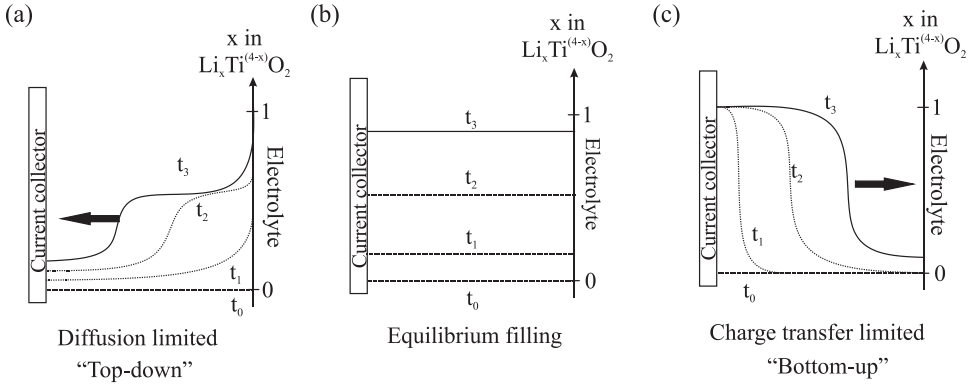

Figure 10. Schematics of Li^+-ion insertion mechanisms. (a) Insertion is limited by diffusion, which leads to buildup of Li within TiO_2 near the electrode-electrolyte interface. In the case of anatase, a $Li_{0.5}TiO_2$ phase moves inwards from the electrolyte interface toward the current collector. (b) Insertion occurs "at equilibrium", without limitation of diffusion or charge-transfer. (c) Insertion is limited by charge transfer, effectively growing the Li_xTiO_2 phase from the current collector to the electrolyte interface.

accommodate, Li will further accumulate at the top of the electrode near the electrode/electrolyte interface (t_3). It is known for anatase that an increase in the Li concentration (above $Li_{0.5}TiO_2$) can lead to a second phase transition (i.e. $LiTiO_2$), resulting in an additional orders of magnitude reduction in Li-ion diffusion coefficient.[44–46] The formation of a blocking $LiTiO_2$ domain is considered the main reason for the limited insertion capacity of anatase.

In general, an insertion mechanism where a small increase in Li concentration leads to a sharp decrease in diffusion coefficient, likely forms a blocking interface near the surface (i.e. at the electrode/electrolyte side). In other words, such a mechanism can be considered a "top-down" filling mechanism. As any additional lithium will further decrease its diffusion, such a mechanism can be considered self-limiting and prevents full capacity utilization of the electrode. Such a top-down insertion mechanism has also been formulated before for "thick" anatase TiO_2 films (135 nm) based on optical and electrochemical results.[28]

Next, it is useful to consider the ideal case of insertion under (near-) equilibrium conditions (Figure 10b). If Li is inserted slowly and without phase-transition, homogenous distribution of Li-ions throughout the electrode can be obtained. At each time (t_{1-3}), the concentration of Li is (nearly) equal across the electrode. This requirement is likely fulfilled for am-TiO_2 during CV scans performed at low scan rate (i.e. 1 mV s^{-1}), since the analysis neither showed diffusion limitations (Figure 4a) nor any influence of overpotentials (Figure 4b).

However, as seen from the CV analysis of am-TiO_2 for higher scan rates, although there was no indication of diffusion limitation, an increasing overpotential was measured. In a system purely controlled by charge transfer kinetics, the overpotential in CV should have a logarithmic dependence on the peak current. In our case, a linear relationship between the peak current and overpotential was measured. From this relationship, an "ohmic" resistance was calculated of about 1.2k Ω cm^{-2}. This value corresponds quite well with the internal resistance determined using PITT (see Figure S5b) for am-TiO_2. This suggests that the largest contribution to the internal resistance is the electrode resistance (R_e), as this would also follow an ohmic behavior.

For our thin-film electrodes, during Li-ion insertion, the corresponding electrons are introduced via the current-collector. If the electronic conductivity is higher than the ionic conductivity, association of Li^+ with an electron (e^-) occurs near electrode/electrolyte interface, as in the case of anatase TiO_2. The neutral Li^+/e^- pair is then primarily transported through the film via diffusion. However, it is known that am-TiO_2 has typically a lower electrical conductivity compared to anatase.[47] Combined with the fact that am-TiO_2 has a higher diffusion coefficient than anatase, a different insertion mechanism is possible. In this case, association of Li^+ with e^- occurs near the current-collector/electrode interface. Li^+ is then transported through the film via migration and associates with e^- near the current-collector.

This situation for am-TiO_2 can be considered a "bottom-up" fill mechanism, as the Li concentration (i.e. Li^+/e^- pair) grows from the current-collector/electrode to the electrode/electrolyte interface. The benefit of such an insertion mechanism is that Li^+ are continuously transported through an "empty" TiO_2 phase. As the diffusion coefficient drops several orders of magnitude as $x \rightarrow 1$, increasing the Li concentration from the bottom up is the most efficient way to fill the electrode. A schematic showing the bottom-up fill is given in Figure 10c. At t_1, Li-ions are transported toward the current collector, and associate with the electron to form the Li_xTiO_2 phase. In this case, $LiTiO_2$ forms at the bottom, and as more Li-ions are inserted (t_2), the $LiTiO_2$ phase grows upwards, until it starts to reach the electrolyte (t_3).

A similar phenomena has been observed for delithiation of $LiFePO_4$ in a solid-state microbattery using scanning transmission X-ray microscopy.[48] By following the Fe^{2+}/Fe^{3+} states within the electrode using X-ray Absorption Near Edge Structure (XANES), the delithiation/lithiation could be followed microscopically. It was shown that during delithiation of $LiFePO_4$, the $FePO_4$ phase grew from the current-collector toward to solid-electrolyte; opposite of what would be expected based on a purely diffusion controlled process. This was explained by the faster Li-ion conductivity within $LiFePO_4$ compared to the electron conductivity. Similar to our case, the enhanced Li-ion conductivity relative to its electron conductivity will lead to a filling mechanism which occurs opposite of where Li^+ is inserted. To further support this hypothesis, it would be interesting to perform in situ XANES with am-TiO_2 films and follow the Ti^{3+}/Ti^{4+} states during lithiation/delithiation.

Conclusions

Amorphous and anatase thin-films were deposited using ALD and characterized for their Li^+-ion insertion properties. From ERDA, differences in composition between am-TiO_2 and anatase were found, with am-TiO_2 having a higher impurity content of H, C and N. This is likely a result of the low deposition temperature used (i.e. 100°C), which was needed to ensure the amorphous nature of the films. During electrochemical testing it was found that an activation step was necessary to obtain good Li-ion insertion properties for am-TiO_2. Only when applying a voltage below 1 V vs Li^+/Li was the am-TiO_2 fully activated. CV experiments revealed a different insertion mechanism between am-TiO_2 and anatase. Whereas a diffusion limited process was measured for anatase, insertion for am-TiO_2 proceeded un-restricted by diffusion. Furthermore, a significantly higher overpotential was required for insertion into anatase compared to am-TiO_2. Constant current lithiation and delithiation experiments revealed a volumetric capacity of am-TiO_2 that was three times the anatase capacity. An exceptional rate-performance was obtained for 35 nm films, with 67% of the maximum capacity reached at a rate of 115 C. The rate-performance was further improved by decreasing the film thickness to 10 or 5 nm TiO_2. For the 5 nm film, the accessible capacity at 500 C was 266 mAh cm^{-3} or 116 mAh g^{-1}, which was 54% its maximum capacity. PITT experiments probed the near-equilibrium thermodynamic and kinetic properties of lithiation and delithiation in am-TiO_2 and anatase. While am-TiO_2 shows lithium insertion and extraction almost across the whole 3.0–0.1 V range, most of the lithiation and delithiation for anatase occurs across near 1.78 V and 1.90 V, respectively. Solid-state Li^+-ion diffusion coefficients and internal electrode resistances were obtained after fitting of PITT current transients to equivalent circuit models. A different trend in D vs U was observed between anatase and am-TiO_2. Using the combination of electrochemical analysis techniques, two different insertion mechanisms were formulated for anatase and am-TiO_2. The sluggish Li^+ diffusion in anatase leads to a buildup of Li_xTiO_2 near the electrode/electrolyte interface, leading to a top-down filling mechanism. In contrast, am-TiO_2 shows fast Li^+ diffusion which leads to the buildup of Li_xTiO_2 from the bottom up, and helps to explain its superior charging capabilities. This work highlights am-TiO_2 as a high rate anode material and shows the benefits of using the amorphous TiO_2 structure.

Acknowledgments

Dr. Shaoren Deng (UGent), under supervision of Prof. Christophe Detavernier (UGent), for ALD of amorphous TiO_2 on TiN substrates. S. M. gratefully acknowledges the support of a Ph.D. stipend from the Agency for Innovation by Science and Technology in Flanders (IWT).

ORCID

S. Moitzheim https://orcid.org/0000-0003-4773-9796
S. De Gendt https://orcid.org/0000-0003-3775-3578

References

1. G. Lui, G. Li, X. Wang, G. Jiang, E. Lin, M. Fowler, A. Yu, and Z. Chen, Flexible, Three-Dimensional Ordered Macroporous TiO_2 Electrode with Enhanced Electrode–electrolyte Interaction in High-Power Li-Ion Batteries, *Nano Energy*, **24**, 72 (2016).

2. J. Ye, A. C. Baumgaertel, Y. M. Wang, J. Biener, M. M. Biener, M. Monika, M. M. Biener, and M. Monika, Structural Optimization of 3D Porous Electrodes for High-Rate Performance Lithium Ion Batteries, *ACS Nano*, **9**, 2194 (2015).
3. H. Yang, C.-K. Lan, and J.-G. Duh, The Power of Nb-Substituted TiO_2 in Li-Ion Batteries: Morphology Transformation Induced by High Concentration Substitution, *J. Power Sources*, **288**, 401 (2015).
4. W. Li, D. Corradini, M. Body, C. Legein, M. Salanne, J. Ma, K. W. Chapman, P. J. Chupas, A.-L. Rollet, C. Julien, K. Zhagib, M. Duttine, A. Demourgues, H. Groult, and D. Dambournet, High Substitution Rate in TiO_2 Anatase Nanoparticles with Cationic Vacancies for Fast Lithium Storage, *Chem. Mater.*, **27**, 5014 (2015).
5. Y. Shen, J. S. Chen, J. Zhu, Q. Yan, and X. Hu, Growth of Two-Dimensional Ultrathin Anatase TiO_2 Nanoplatelets on Graphene for High-Performance Lithium-Ion Battery, *J. Nanoparticle Res*, **15**, 1913 (2013).
6. J. Liu, J. S. Chen, X. Wei, X. W. Lou, and X. Liu, Sandwich-Like, Stacked Ultrathin Titanate Nanosheets for Ultrafast Lithium Storage, *Adv. Mater.*, **23**, 998 (2011).
7. G. Armstrong, A. R. Armstrong, P. G. Bruce, P. Reale, and B. Scrosati, TiO_2(B) Nanowires as an Improved Anode Material for Lithium-Ion Batteries Containing $LiFePO_4$ or $LiNi_{0.5}Mn_{1.5}O_4$ Cathodes and a Polymer Electrolyte. Adv. Mater., **18**, 2597 (2006).
8. H. Xiong, H. Yildirim, E. V Shevchenko, V. B. Prakapenka, B. Koo, M. D. Slater, M. Balasubramanian, S. K. R. S. Sankaranarayanan, J. P. Greeley, S. Tepavcevic, N. M. Dimitrijevic, P. Podsiadlo, C. S. Johnson, and T. Rajh, Self-Improving Anode for Lithium-Ion Batteries Based on Amorphous to Cubic Phase Transition in TiO_2 Nanotubes, *J. Phys. Chem. C*, **116**, 3181 (2012).
9. H. Fang, M. Liu, D. Wang, T. Sun, D.-S. Guan, F. Li, J. Zhou, T.-K. Sham, and H.-M. Cheng, Comparison of the Rate Capability of Nanostructured Amorphous and Anatase TiO_2 for Lithium Insertion Using Anodic TiO_2 Nanotube Arrays, *Nanotechnology*, **20**, 225701 (2009).
10. W. J. H. Borghols, D. Lützenkirchen-Hecht, U. Haake, W. Chan, U. Lafont, E. M. Kelder, E. R. H. van Eck, A. P. M. Kentgens, F. M. Mulder, and M. Wagemaker, Lithium Storage in Amorphous TiO_2 Nanoparticles, *J. Electrochem. Soc.*, **157**, A582 (2010).
11. S. Moitzheim, J. E. Balder, P. Poodt, S. Unnikrishnan, S. De Gendt, and P. M. Vereecken, Chlorine Doping of Amorphous TiO_2 for Increased Capacity and Faster Li^+-Ion Storage, *Chem. Mater.*, **29**, 10007 (2017).
12. S. Moitzheim, C. S. Nimisha, S. Deng, D. J. Cott, C. Detavernier, and P. M. Vereecken, Nanostructured TiO_2/Carbon Nanosheet Hybrid Electrode for High-Rate Thin-Film Lithium-Ion Batteries, *Nanotechnology*, **25**, 504008 (2014).
13. M. Li, X. Li, W. Li, X. Meng, Y. Yu, and X. Sun, Atomic Layer Deposition Derived Amorphous TiO_2 Thin Film Decorating Graphene Nanosheets with Superior Rate Capability, *Electrochem. commun.*, **57**, 43 (2015).
14. M. Xie, X. Sun, C. Zhou, A. S. Cavanagh, H. Sun, T. Hu, G. Wang, J. Lian, and S. M. George, Amorphous Ultrathin TiO_2 Atomic Layer Deposition Films on Carbon Nanotubes as Anodes for Lithium Ion Batteries, *J. Electrochem. Soc*, **162**, A974 (2015).
15. X. H. Wang, C. Guan, L. M. Sun, R. A. Susantyoko, H. J. Fan, and Q. Zhang, Highly Stable and Flexible Li-Ion Battery Anodes Based on TiO_2 Coated 3D Carbon Nanostructures, *J. Mater. Chem. A*, **3**, 15394 (2015).
16. J. Song and W. West, All Solid-State Thin Film Batteries, In Handbook of Solid State Batteries, N. J. Dudney, W. C. West, J. Nanda, *Eds.; Materials and Energy; World Scientific*, 2015; Vol. **6**, pp 591.
17. Y. Chen, Y. Zhang, B. Chen, Z. Wang, and C. Lu, An Approach to Application for $LiNi_{0.6}Co_{0.2}Mn_{0.2}O_2$ Cathode Material at High Cutoff Voltage by TiO_2 Coating, *J. Power Sources*, **256**, 20 (2014).
18. W. Liu, M. Wang, X. L. Gao, W. Zhang, J. Chen, H. Zhou, and X. Zhang, Improvement of the High-Temperature, High-Voltage Cycling Performance of $LiNi_{0.5}Co_{0.2}Mn_{0.3}O_2$ Cathode with TiO_2 Coating, *J. Alloys Compd.*, **543**, 181 (2012).
19. H. C. M. Knoops, L. Baggetto, E. Langereis, M. C. M. van de Sanden, J. H. Klootwijk, F. Roozeboom, R. A. H. Niessen, P. H. L. Notten, and W. M. M. Kessels, Deposition of TiN and TaN by Remote Plasma ALD for Cu and Li Diffusion Barrier Applications, *J. Electrochem. Soc.*, **155**, G287 (2008).
20. Q. Xie, Y.-L. Jiang, C. Detavernier, D. Deduytsche, R. L. Van Meirhaeghe, G.-P. Ru, B.-Z. Li, and X.-P. Qu, Atomic Layer Deposition of TiO_2 from Tetrakis-Dimethyl-Amido Titanium or Ti Isopropoxide Precursors and H_2O, *J. Appl. Phys.*, **102**, 083521 (2007).
21. V. Pore, A. Rahtu, M. Leskelä, M. Ritala, T. Sajavaara, and J. Keinonen, Atomic Layer Deposition of Photocatalytic TiO_2 Thin Films from Titanium Tetramethoxide and Water, *Chem. Vap. Depos.*, **10**, 143 (2004).
22. S. Giangrandi, T. Sajavaara, B. Brijs, K. Arstila, A. Vantomme, and W. Vandervorst, Low-Energy Heavy-Ion TOF-ERDA Setup for Quantitative Depth Profiling of Thin Films, *Nucl. Instruments Methods Phys. Res. B*, **266**, 5144 (2008).
23. M. Laitinen, M. Rossi, J. Julin, and T. Sajavaara,Time-of-Flight – Energy Spectrometer for Elemental Depth Profiling – Jyväskylä Design, *Nucl. Instruments Methods Phys. Res. B*, **337**, 55 (2014).
24. C. R. Ottermann and K. Bange, Correlation between the Density of TiO_2 Films and Their Properties, *Thin Solid Films*, **286**, 32 (1996).
25. J. S. Chen and X. W. Lou, Anatase TiO_2 Nanosheet: An Ideal Host Structure for Fast and Efficient Lithium Insertion/Extraction, *Electrochem. commun.*, **11**, 2332 (2009).
26. T. Dobbelaere, F. Mattelaer, J. Dendooven, P. Vereecken, and C. Detavernier, Plasma-Enhanced Atomic Layer Deposition of Iron Phosphate as a Positive Electrode for 3D Lithium-Ion Microbatteries, *Chem. Mater.*, **28**, 3435 (2016).
27. K. B. Gandrud, A. Pettersen, O. Nilsen, and H. Fjellvåg, High-Performing Iron Phosphate for Enhanced Lithium Ion Solid State Batteries as Grown by Atomic Layer Deposition, *J. Mater. Chem. A*, **1**, 9054 (2013).
28. R. van de Krol, A. Goossens, J. Schoonman, R. Van De Krol, A. Goossens, J. Schoonman, R. van de Krol, A. Goossens, and J. Schoonman, Spatial Extent of Lithium Intercalation in Anatase TiO_2, *J. Phys. Chem. B*, **103**, 7151 (1999).
29. K. Aoki, K. Tokuda, and H. Matsuda, Theory of Linear Sweep Voltammetry with Finite Diffusion Space, *J. Electroanal. Chem. Interfacial Electrochem.*, **160**, 33 (1984).
30. S.-I. Pyun, H.-C. Shin, J.-W. Lee, J.-Y. Go, and Electrochemical Methods, In Electrochemistry of Insertion Materials for Hydrogen and Lithium, F. Scholz, Ed., Springer-Verlag: Heidelberg, 2012, pp 11.
31. M. Wagemaker, W. J. H. Borghols, and F. M. Mulder, Large Impact of Particle Size on Insertion Reactions. A Case for Anatase Li_xTiO_2, *J. Am. Chem. Soc.*, **129**, 4323 (2007).
32. M. D. Levi and D. Aurbach, Potentiostatic and Galvanostatic Intermittent Titration Techniques. In *Characterization of Materials*, E. N. Kaufmann, Ed., *John Wiley & Sons: Hoboken*, 2012, pp 913.
33. C. J. Wen, B. A. Boukamp, R. A. Huggins, and W. Weppner, Thermodynamic and Mass Transport Properties of "LiAl." *J. Electrochem. Soc.*, **126**, 2258 (1979).
34. M. Levi and D. Aurbach, Frumkin Intercalation Isotherm — a Tool for the Description of Lithium Insertion into Host Materials: A Review, *Electrochim. Acta*, **45**, 167 (1999).
35. C. Montella, Apparent Diffusion Coefficient of Intercalated Species Measured with PITT: A Simple Formulation, *Electrochim. Acta*, **51**, 3102 (2006).
36. M. A. Vorotyntsev, M. D. Levi, and D. Aurbach, Spatially Limited Diffusion Coupled with ohmic Potential Drop and/or Slow Interfacial Exchange: A New Method to Determine the Diffusion Time Constant and External Resistance from Potential Step (PITT) Experiments, *J. Electroanal. Chem.*, **572**, 299 (2004).
37. M. D. Levi, R. Demadrille, A. Pron, M. A. Vorotyntsev, Y. Gofer, and D. Aurbach, Application of a Novel Refinement Method for Accurate Determination of Chemical Diffusion Coefficients in Electroactive Materials by Potential Step Technique, *J. Electrochem. Soc.*, **152**, E61 (2005).
38. C. Montella and J.-P. Diard, New Approach of Electrochemical Systems Dynamics in the Time-Domain under Small-Signal Conditions. I. A Family of Algorithms Based on Numerical Inversion of Laplace Transforms, *J. Electroanal. Chem.*, **623**, 29 (2008).
39. C. Montella, Re-Examination of the Potential-Step Chronoamperometry Method through Numerical Inversion of Laplace Transforms. I. General Formulation and Numerical Solution, *J. Electroanal. Chem.*, **633**, 35 (2009).
40. C. Montella, Re-Examination of the Potential Step Chronoamperometry Method through Numerical Inversion of Laplace Transforms. II. Application Examples. *J. Electroanal. Chem.*, **633**, 45 (2009).
41. Mathematica Version, **10**.2. Wolfram Research: Champaign, IL 2015.
42. C. Montella and R. Michel, New Approach of Electrochemical Systems Dynamics in the Time Domain under Small-Signal Conditions: III - Discrimination between Nine Candidate Models for Analysis of PITT Experimental Data from Li_xCoO_2 Film Electrodes, *J. Electroanal. Chem.*, **628**, 97 (2009).
43. J. S. Chen, J.-P. Diard, R. Durand, and C. Montella, Hydrogen Insertion Reaction with Restricted Diffusion. Part 1. Potential Step—EIS Theory and Review for the Direct Insertion Mechanism, *J. Electroanal. Chem.*, **406**, 1 (1996).
44. M. Koudriachova, N. Harrison, and S. de Leeuw, Effect of Diffusion on Lithium Intercalation in Titanium Dioxide, *Phys. Rev. Lett.*, **86**, 1275 (2001).
45. A. A. Belak, Y. Wang, and A. Van der Ven, Kinetics of Anatase Electrodes: The Role of Ordering, Anisotropy, and Shape Memory Effects, *Chem. Mater.*, **24**, 2894 (2012).
46. M. Wagemaker, D. Lützenkirchen-Hecht, A. A. van Well, and R. Frahm ,Atomic and Electronic Bulk versus Surface Structure: Lithium Intercalation in Anatase TiO_2, *J. Phys. Chem. B*, **108**, 12456 (2004).
47. W. S. Shih, S. J. Young, L. W. Ji, W. Water, and H. W. Shiu, TiO_2-Based Thin Film Transistors with Amorphous and Anatase Channel Layer, *J. Electrochem. Soc.*, **158**, H609 (2011).
48. N. Ohmer, B. Fenk, D. Samuelis, C. Chen, J. Maier, M. Weigand, E. Goering, and G. Schu, Phase Evolution in Single-Crystalline $LiFePO_4$ Followed by in Situ Scanning X-Ray Microscopy of a Micrometre-Sized Battery, *Nat. Commun.*, **6**, 1 (2015).